JOURNAL OF SPACECRAFT AND ROCKETS
Vol. 45, No. 3, May–June 2008

Numerical Investigation of a Spiked Blunt Nose Cone at Hypersonic Speeds

M. Gauer* and A. Paull†
University of Queensland, Brisbane, Queensland 4072, Australia

DOI: 10.2514/1.30590

When flying at hypersonic speeds, it is a fundamental requirement to reduce the high drag resulting from a blunt nose cone in the ascent stage to increase the payload weight on the one hand and decrease the amount of energy needed to overcome the Earth's gravity on the other. However, an aerospike can be attached on the front of the nose cone to obtain a high drag and heat load reduction. Different Mach numbers at different altitudes have been chosen to investigate the effect of the aerospike on the nose cone's surrounding flowfield. The drag and the heat load reduction is numerically evaluated at Mach numbers of 5.0, 7.0, and 10.0. Different lengths of the aerospike are investigated between 1 and 4 times the diameter of the dome of the nose cone. Additional modifications to the tip of the spike to obtain different bow shocks are examined, including a sharp front, a blunt spike, and an aerodome mounted on the tip of the spike. To solve the very complicated flowfield, the flow solver CFD-FASTRAN is used.

Nomenclature

A	=	area, m^2
A_f, A_b	=	frequency factor of forward, backward reaction
c	=	speed of sound, m/s
D	=	diameter of the dome of the nose cone, m
d	=	diameter of the aerodome, m
dp/dx	=	pressure gradient in the streamwise direction
dp/dy	=	pressure gradient normal to the wall
E	=	activation energy
H	=	altitude, km
L	=	length of the aerospike, m
M	=	Mach number
Pr	=	Prandtl number
p	=	pressure, N/m^2
q	=	heat flux, W/m^2
R	=	radius, m
Re_D	=	Reynolds number based on the diameter
T	=	temperature, K
U	=	velocity, m/s
u, v	=	streamwise, wall-normal velocity, m/s
x, y	=	streamwise, wall-normal direction
y^+	=	nondimensional wall distance
α	=	separation angle of the recirculation area, deg
Δ_0	=	shock stand-off distance, m
ε	=	entropy fix
γ	=	ratio of specific heats
λ	=	eigenvalue
μ	=	viscosity, Ns/m^2
ρ	=	density, kg/m^3

Subscripts

b	=	backward reaction
f	=	forward reaction
max	=	maximum
w	=	wall
∞	=	freestream value
1	=	ahead of the shock wave
2	=	behind the shock wave

Received 21 March 2007; revision received 14 November 2007; accepted for publication 27 November 2007.

*Research Assistant, German Aerospace Center, Spacecraft Section, Bunsenstraße 10, 37073 Göttingen, Germany.

†Research Leader, Applied Hypersonics, Weapons Systems Division, Defence Science and Technology Organisation Brisbane, Post Office Box 883, Queensland 4069, Australia.

I. Introduction

THE drag of hypersonic vehicles and missiles plays a very important role in their final performance and hence in their design. Ogival noses were mainly used in former missile designs due to their good drag characteristics, but the volumetric efficiency is poor compared with the shape of a hemisphere. Several techniques have been developed with the target of significantly reducing the aerodynamic drag of blunt nose cones. Experiments involving supersonic projectiles fired upstream in the flow from the stagnation point, the feed in of concentrated energy along the stagnation streamline, and even beamed laser and microwave energy focused to a specific point in front of the nose cone [1,2] have been conducted to avoid mounting an aerospike at the tip of the nose cone. Nevertheless, out of all of the investigated drag-reducing techniques, the use of a forward-facing spike attached to the nose cone of the hypersonic vehicle appears to be the most effective and simplest method.

The shock wave angle decreases with an increasing Mach number. Such thin shock layers can cause the front shock to impinge on the downstream surfaces of the investigated geometry. For short length aerospikes with one times the diameter of the dome, which are among other things investigated in this paper, the spike-induced bow shock can hit the dome of the nose cone. This can cause severe heating problems, which have to be taken into account when designing the affected parts.

The experimental investigations of the flowfield around a spiked–blunt body began in the 1950s. Stalder and Nielsen [3] examined the heat transfer and the pressure distribution of a hemisphere cylinder equipped with a sharp aerospike. Their tests were conducted with a maximum Mach number of 5.04 and thus slightly grazed the hypersonic regime. Their best configuration delivered a drag reduction of 45%. Moreover, when the flow is supersonic, that is, at a Mach number of about 2, the recirculation area in front of the dome was not considerably useful because the heat loads on the top of the dome were higher with the spike than without. This can be ascribed to the turbulent separated region impinging periodically on the outer edge of the boundary layer of the blunt nose.

Bogdonoff and Vas [4] examined instead whether a significant drop in heat transfer to the body would result if the flow in the

recirculation area remained laminar. Their investigations have shown that the longer the spike is extended, the more drag reduction can be achieved.

Chapman [5] also found a reduction in heat transfer of 56% across the separated laminar boundary layer compared with the attached boundary layer. The effect of the spike length on the nose cone's pressure distribution and the heat flux was also experimentally investigated by Crawford [6]. His experiments were accomplished with a fixed Mach number of 6.8 and a varying Reynolds number based on the cylinder diameter. The investigations, which yielded the same results as previous studies, also showed that there is no further reduction of drag when the spike length exceeds roughly 4 times the diameter of the body.

Interesting results can also be obtained from Wood's [7] examinations of spiked cones. He came to the conclusion that the shape and size of the recirculation area is primarily controlled by the flowfield in the vicinity of the reattachment point.

Reding et al. [8] investigated the effects of the fluctuating pressure in the flow separation region on the aerodynamic damping of the Trident I missile. It emerged that the spike has an adverse effect on the aerodynamic damping. The Apollo-Saturn boosters, for example, damp several critical modes with their tail fins and thereby provide the aeroelastic stability. Here, the escape rocket produces a comparable flowfield to that of an aerospike.

The knowledge of hypersonic aerodynamic spike flow effects was extended by Hutt and East [9], who examined the effects of a spike on the pitch stability of a blunted cone. They concluded that for both zero and nonzero angles of attack the aerospike can significantly influence the stiffness and damping of a hypersonic vehicle.

Because the benefits of aerospikes are also highly interesting for missiles of certain ranges, their influence on the drag when flying with angles of attack has also been examined. A detailed investigation of angles of up to 40 deg was undertaken by Huebner et al. [10]. Their experiments have shown that the aerospike is only beneficial in a specific range of the vehicle's angle of attack. The limiting factor is the impact of the separation shock on the dome, which leads to high pressure and temperature rises.

Serious numerical investigations of spiked–blunt body flow began in the late 1980s. Shoemaker [11], Fujita and Kubota [12], Yamauchi et al. [13], Mehta [14,15], and Kamran et al. [16] used different codes and software to solve the compressible viscous Navier-Stokes equations. Several simulations focused on the validation of the numerical code by comparing the computed results to prior experimentally investigated aerospike-induced flowfields.

The flowfield induced by the forward-facing aerospike is shown in Fig. 1. It is characterized by a conical shock wave initiated from the front of the aerospike, a recirculation area in front of the blunt nose cone, a flow separation shock that separates the inviscid flow from the recirculation region, and finally a reattachment shock wave resulting from the blunt nose cone. The dynamic pressure in the recirculation area is highly reduced and thus leads to the decrease in drag and heat load on the surface. Consequently, the geometry, that is, the length and shape of the spike, has to be suitably chosen to obtain a large conical recirculation area in front of the dome to get maximum drag reduction.

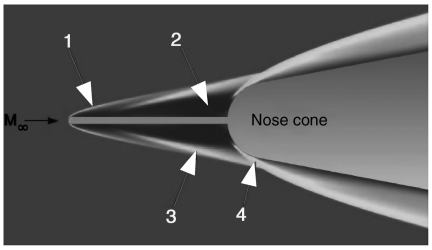

Fig. 1 Aerospike-induced flowfield: 1) spike bow shock, 2) recirculation area, 3) flow separation shock, and 4) reattachment shock.

II. Computational Grid

A. Geometry

The geometry of the nose cone is determined by the size of the payload of the investigated vehicle and is therefore fixed. The shape and the length of the aerospike are chosen by the author.

The following different geometries of the aerospike are numerically investigated in the scope of this paper. They vary in both length and shape. In all cases, the shaft of the spike is a cylinder with the diameter $0.1D$, where D stands for the diameter of the dome of the nose cone.

The most common shape for the front of the spike is shown in Fig. 2, as also investigated by Stalder and Nielsen [3], Bogdonoff and Vas [4], Wood [7], Fujita and Kubota [12], Mehta [14,15], and Thurman [17] but with varying angles of the front cone. The length L of the aerospike varies from 0.3 to 1.2 m, which conforms to a ratio of L/D from 1 up to 4, where D is the diameter of the dome of the nose cone. Spikes longer than 4 times the diameter of the nose cone are not investigated. Experimental investigations from Bogdonoff and Vas [4] and Crawford [6] emphasized that the beneficial effect remains unaffected when the spike length exceeds $L/D = 4$.

To reduce the heat loads on the tip of the aerospike, the front cone from the sharp spike is replaced with a simple dome ($q_w \sim 1/R^{0.5}$ [18], where q_w is the heat flux in the wall and R is the radius of the dome) illustrated in Fig. 3. Additionally, the blunt tip causes a stronger shock that results in a wider bowed shock front. This in turn reduces the probability of an impingement of the spike-induced shock on surfaces located further downstream.

To decrease the heat flux even more and to get a wider bow shock compared with the blunt spike, an aerodome as illustrated in Figs. 4 and 5 is mounted on the tip of the spike. The ratio D/d describes the ratio of the diameter D of the dome of the nose cone to the diameter d of the aerodome.

By using the aerodome, the resultant wider bow shock should make it possible to use shorter lengths for the aerospike but to gain the same drag reduction as obtained with the blunt or sharp spike. The connection from the aerodome with $D/d = 3$ to the shaft is solved with a steeper angle when compared with the aerodome with $D/d = 4$ to get a second recirculation area behind the dome and to investigate the effect of this area on the surrounding flowfield.

B. Grid Generation

Only half of the geometry needs to be modeled because the flow is assumed to be axisymmetric as no angles of attack are considered in the present analysis. The structured grid generation is based on the transfinite interpolation methodology. These types of grids use quadrilateral elements in 2-D in the computational array. The quadrilateral elements, which are very efficient at filling space, support a high amount of skew and stretching before the solution will be significantly affected. Additionally, the grid can be aligned with the flow, thereby yielding greater accuracy within the solver. Figures 6 and 7 show a more detailed view of the adapted grid in front of the aerodome and the spiked nose cone.

The outer boundary of all grids is adapted to the shock wave initiated from the tip of the spike or the blunt nose cone, respectively.

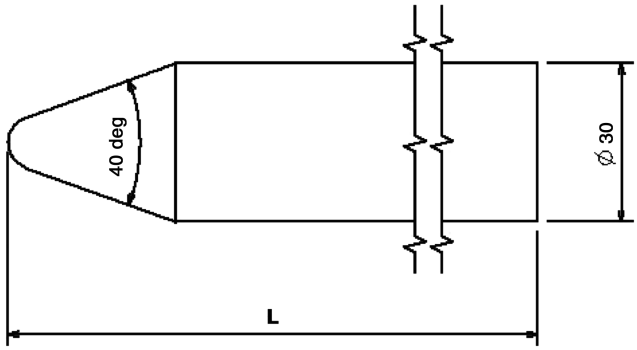

Fig. 2 Sharp spike.

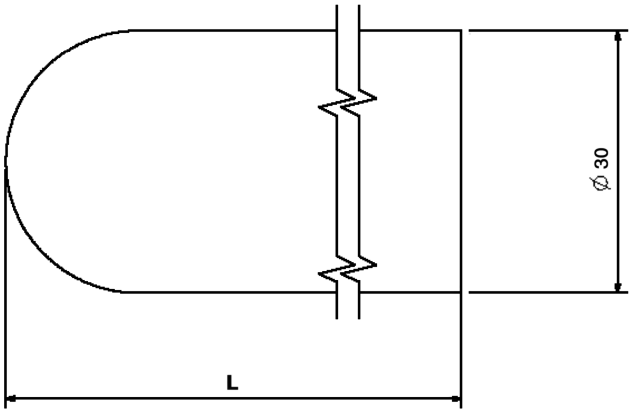

Fig. 3 Blunt spike.

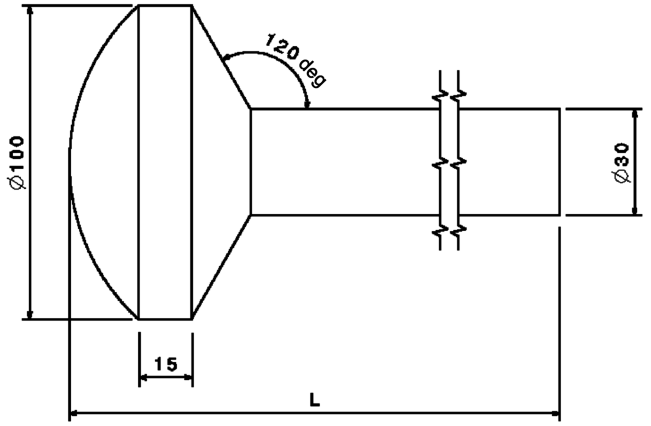

Fig. 4 Aerodome with $D/d = 3$.

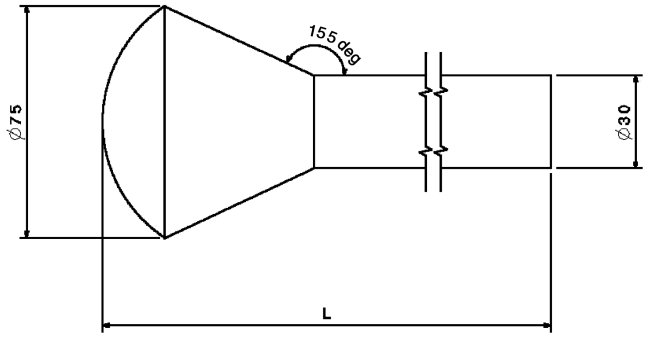

Fig. 5 Aerodome with $D/d = 4$.

This has been considered to be the best option to get a smooth grid that is "flowing" with the shock. Outer boundaries as chosen, for example, by Shoemaker [11], Yamauchi et al. [13], Mehta [14], and Kamran et al. [16], that is, a rectangular mesh boundary, inclined boundaries, or a semicircle at the front, result in skewed grid cells that may lead to a decreased quality of the numerical solution.

To verify that the chosen grid delivers an accurate solution, the number of grid cells was increased until a steady solution occurred, that is, the resulting force on the investigated shape did not change anymore. Several test runs were made with a total doubled grid cell number. Therefore, the grid was highly refined in both directions. Grids are chosen with the number of grid points in the i direction ranging from 247 for the shortest blunt spike to up to 370 for the longest aerodome configuration, and the number in the j direction ranging from 152 to 183. Simulations with higher grid cell numbers delivered nonchanging results.

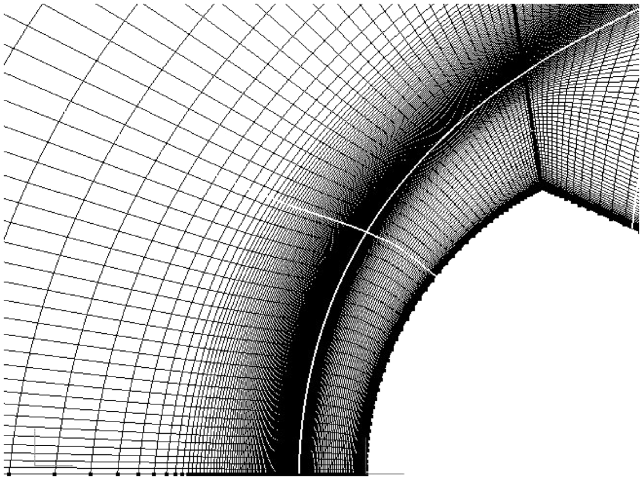

Fig. 6 Adapted grid in front of the aerodome.

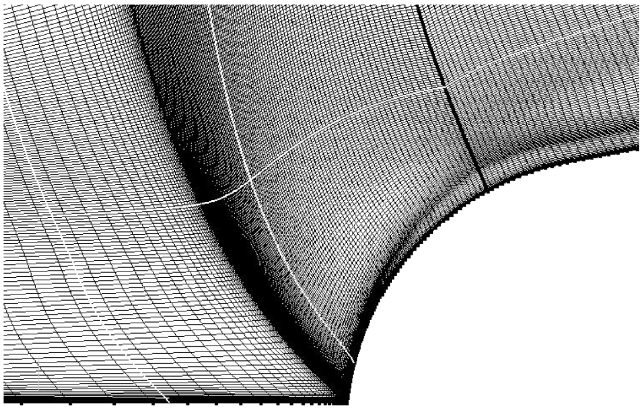

Fig. 7 Adapted grid in front of the spiked nose cone.

However, the grid adaptation is of great importance for the accuracy of the result. Nonadapted and skewed grids showed significant discrepancies, even with a doubled grid cell number. The results were fluctuating and hence nonrepresentative.

C. Grid Spacing

The numerical computation of a viscous flowfield demands of course a bigger number of grid cells because the boundary layer has to be solved properly to take the viscous effects at the wall into account. The grid spacing in the stagnation point of the unspiked nose cone and the aerodome is chosen with 1×10^{-6} m. Because the boundary layer thickens with running length, the grid spacing at the very end of the nose cone increases to 1×10^{-5} m. Test runs revealed that this grid spacing is sufficient to resolve the viscous effects.

However, another criterion is included to validate the grid size at the wall. This criterion is based on the constraint that the first grid cell above the wall has to be within a certain range of the nondimensional wall distance y^+, where y^+ is the inner scaling for a turbulent boundary layer. To resolve the viscous effects properly, the first grid cell must be located within a y^+ value of 1 (see Wilcox [19]). The first grid cell in all generated grids is located between $0.1 \leq y^+ \leq 0.5$ in reference to the turbulent scaling, dependent on the Mach number of the case and on the running length.

The total number of grid cells reaches from 24964 for the unspiked nose cone up to 64206 cells for the longest aerodome assembly.

III. Flow Solver Settings

A. Model Options and Flow Properties

In the global settings of the CFD-FASTRAN solver, the problem is defined as axisymmetric, which yields the complete geometry by

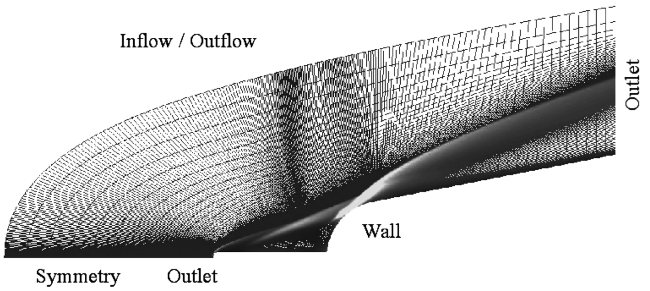

Fig. 8 Boundary condition types as defined for the simulations.

one angular rotation about the x axis. The axisymmetric computations are done by revolving the grid about the x axis by 4 deg.

The solver uses a time-marching procedure to calculate the flow. The flow is defined to be steady because the flowfield is converging to a steady state. The steady option uses local time stepping, which leads to a faster convergence to the steady-state flowfield.

Crawford [6] experimentally investigated the flowfield around a spiked–blunt body for Reynolds numbers in the range of 0.12×10^6–1.5×10^6, based on the cylinder diameter. According to his analyses, the flow in this range can be assumed to be laminar. The maximum Reynolds number occurring in the performed simulations is given with $Re_D \approx 1.2 \times 10^6$. Thus, the flow is assumed to be laminar, which is also consistent to Bogdonoff and Vas [4], Fujita and Kubota [12], Yamauchi et al. [13], and Boyce et al. [20].

The viscosity is not set as being constant but is computed with the help of Sutherland's law. The Prandtl number is set to $Pr = 0.71$.

B. Boundary and Initial Conditions

The types of boundary conditions for the grid are defined as shown in Fig. 8. The conditions that apply to the inflow boundary are derived from the three chosen mission points out of the nominal trajectory of the investigated vehicle and are listed in Table 1.

All variables from the interior of the domain are extrapolated to the outlet boundary. The surface of the models are defined to be isothermal at a temperature of $T_w = 300$ K for all investigated mission points. No slip wall conditions, that is, $u_w = v_w = 0.0$, were applied to the viscous surfaces of the models [12,13,15,16,21]. Because the flow in front of the bow shock remains unchanged, parts of the lower left boundary in Fig. 8 are chosen as a symmetry-type boundary. This selection makes the numerical simulation slightly quicker because no extrapolation is necessary.

A faster convergence can be achieved, and thus a shorter computation time, when the initial conditions are chosen as close as possible to the final steady-state values. However, the highly complicated flowfield, which is characterized by several different flow zones, makes it impossible to adapt the initial conditions close to the steady-state values. Therefore, the initial conditions are defined to be equal to the freestream values [12–16].

C. Solver Settings

The residuals of the density and the total energy of the flow can be monitored in FASTRAN, which allows the user to monitor if the convergence criterion has been chosen properly. The convergence criterion in all simulations is defined with 1×10^{-5}.

Table 1 Flow variables for the inflow/outflow boundary condition

	Mission point I	Mission point II	Mission point III
M	5	7	10
H, km	25	31	71
U_∞, m/s	1492.14	2117.08	2937.14
p_∞, N/m^2	2510	1008.3	3.95674
T_∞, K	221.65	227.65	214.65
μ_∞, Ns/m^2	1.45×10^{-5}	1.48×10^{-5}	1.41×10^{-5}

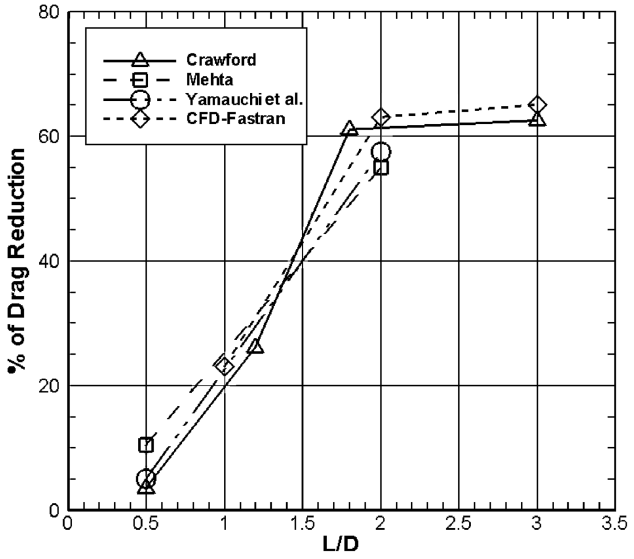

Fig. 9 Comparison of the drag reduction between FASTRAN, Crawford [6], Mehta [14] and Yamauchi et al. [13].

To prevent and to control the appearance of spurious oscillations resulting from regions with large gradients, the introduction of flux difference splitting is implemented. Roe's approximate Riemann solver is used, which, however, may result in a discontinuity in the expansion fan. This disadvantage of Roe's scheme can be minimized by using the entropy fix. The fix can be described as

$$\lambda_i = \max(\lambda_i, \varepsilon \cdot \lambda_{\max}) \quad \text{with} \quad \lambda_{\max} = V + c \tag{1}$$

where λ_i represents the eigenvalues of the system and ε is specified by the user. Suggested values for the entropy fix are 0.1–0.3, where $\varepsilon = 0.3$ is chosen for the simulations. The velocity magnitude plus the speed of sound equals the maximum eigenvalue $\lambda_{\max}$.

To obtain a better spatial accuracy, the second-order flux limiter minmod is used. The oscillations at discontinuities, which would be produced by second-order schemes, are completely avoided by this flux limiter. The Point–Jacoby fully implicit scheme is used for all simulations. Fully implicit schemes are inherently stable for linear systems and are currently preferred for viscous compressible flows [22].

It is possible to change the time-step size in the course of the simulation by defining an initial and a final Courant–Friedrichs–Lewy (CFL) number. The CFL number defines the progress in grid cells of the considered size for one time step. To handle the strong nonlinearities that occur in the first few cycles of the simulation, the initial CFL number is set to CFL = 1E − 4. The time-step size will ramp up during the calculation to its final value, which is defined as CFL = 1.

D. FASTRAN Validation

The validation of CFD-FASTRAN is realized with a numerical simulation of Crawford's [6] experimental test runs. In addition, the bow shock stand-off distance of the unspiked nose cone is compared with analytical calculations for all investigated freestream conditions.

Figure 9 shows the comparison of the drag reduction to the unspiked nose cone for a freestream Mach number of 6.8 between CFD-FASTRAN, Crawford's [6] experimental results, and the numerical results of Yamauchi et al. [13] and Mehta [14]. It can be seen that FASTRAN delivers very good results when compared with the other investigations. The error lies within 4% compared with Crawford's results, although the accuracy of his investigations is unknown. The obtained drag reduction exhibits at every investigated spike length a slightly higher level compared with Crawford, which may be ascribed to numerical discrepancies and possible inaccuracies in measured data. However, FASTRAN delivers with

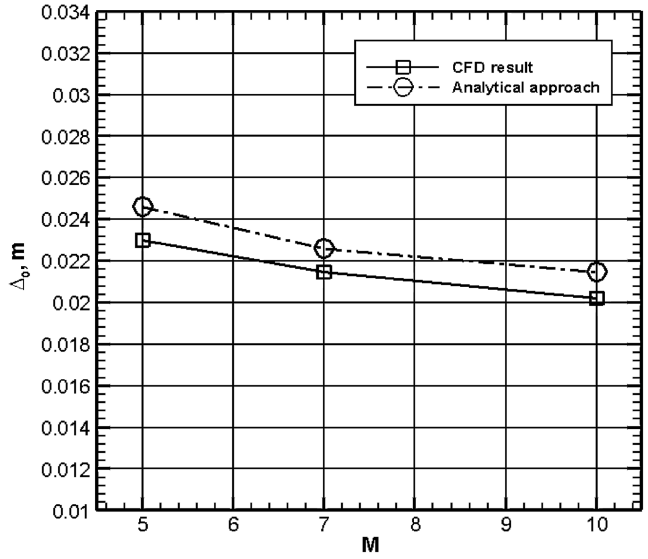

Fig. 10 Comparison between the numerical and analytical shock stand-off distance.

the results of Yamauchi et al. the most representative numbers for the investigated test case.

The detached bow shock is a typical property of the flow around a blunt body. It can be described with the shock stand-off distance Δ_0. For the purpose of a comparison with the CFD result, the bow shock stand-off distance can be analytically approximated. This topic, among others, has been given a lot of attention by Wen and Hornung [23]. In their publication they extended previous studies about the connection between dissociation-nonequilibrium effects in supersonic flows over blunt bodies. The bow shock stand-off distance can be described with

$$\Delta_0 = \frac{LD\rho_1}{\rho_2} \tag{2}$$

where L is a constant factor and represents the solution of Van Dyke, which yields $L = 0.41$ for a sphere. (The reader is referred to Wen and Hornung for a detailed derivation and more information.) As illustrated in Fig. 10, the analytical approach delivers slightly higher values. This can, among other things, be related to the analytical simplification of the constant density assumption behind the shock wave.

E. Additional Settings due to the Consideration of Real Gas Effects

The influence of real gas effects is only considered and relevant in simulations in which the temperature is high enough to start dissociation. The chemical reactions are chosen so that the dissociation of oxygen and also of nitrogen are taken into account. The reactions and their forward and backward reaction rate parameters, which are calculated via Arrhenius law, are listed in Table 2 and are obtained from Park [24]. The third-body efficiencies for the reactions, which include the species M, are given in Table 3 [25]. These efficiencies define by which factor the preexponential factor A in Table 2 has to be multiplied when the corresponding species act as a third body. The species and their mass fractions are specified as shown in Table 3, also obtained from Park [24].

The surface of the investigated bodies can behave as a third body that influences the recombination reactions of the species near the wall. This is called a catalytic surface reaction. It highly influences the thermal state of the surface, that is, the wall temperature and the heat loads can differ remarkably. The worst case with regard to the heat flux is given when the wall is assumed to be fully catalytic, because chemical energy is exchanged partly into thermal energy, which causes a heating of the wall. At a fully catalytic wall, all atoms are assumed to recombine. The chemical reactions are catalyzed at an infinite rate, which means that the mass fraction of the species at the wall is equal to its local equilibrium value with the local pressure and temperature. When the surface is cold enough, a fully catalytic recombination can be expected.

The gas-kinetic thermal state of the gas must also be prescribed. Either thermal equilibrium or two-temperature thermal nonequilibrium must be selected. It is known that any readjustment to the equilibrium state requires a specific length of time. This relaxation time comes from the excitation by collisions, because every redistribution of molecular internal energy demands a number of collisions. Even though the majority of the flowfield is in an equilibrium state, which is especially true for the mission point I flight conditions, it has to be considered that the present flowfield is also characterized by a region in which a nonequilibrium is given, namely, directly behind the bow shock. This in turn leads to the need to implement the equations for nonequilibrium flow. The selection of the thermal nonequilibrium activates an additional energy equation in the solver that has to be considered, namely, the internal energy equation.

With chemical effects, the flow is not modeled with the ideal gas model but with the species gas model, which implies that a mixture of ideal gases is given in the flow. For reacting cases, the viscosity is calculated by formulas derived from kinetic theory considerations. The solver uses Lennard–Jones potentials, the collision integrals, and the characteristic molecular diameters to obtain the species viscosity. To obtain the mixture viscosity, Wilke's semi-empirical formula is used, which in turn implements the species viscosity.

The model for the molecular thermal conductivity for reacting flow is also obtained from the kinetic theory. To determine the conductivities of the species, the species viscosities in conjunction with Eucken's assumption have to be used. Finally, the model for the

Table 2 Chemical reactions and reaction rate parameters

No.	Reaction	A^f	η^f	$(E/R_u)^f$	A^b	η^b	$(E/R_u)^b$
1	$N_2 + M \leftrightarrow 2N + M$	3.716E + 18	−1.6	113,200	2.065E + 11	−1.6	0.0
2	$O_2 + M \leftrightarrow 2O + M$	2.758E + 16	−1	59,400	2.3E + 007	−0.5	0.0
3	$NO + M \leftrightarrow N + O + M$	2.307E + 14	−0.5	75,500	5.767E + 7	−0.5	0.0
4	$N2 + O \leftrightarrow NO + N$	3.192E + 10	0.1	37,500	1.217E + 10	0.1	0.0
5	$NO + O \leftrightarrow O_2 + N$	1.602E + 6	1.29	19,700	3.132E + 5	1.29	3.6E + 3

Table 3 Third-body efficiencies for reactions 1, 2, and 3 in Table 2, and the species mass fractions

Species name	Efficiency for reaction no. 1	Efficiency for reaction no. 2	Efficiency for reaction no. 3	Mass fraction
N	3	3	2	0.001
N_2	1	1	1	0.747
NO	1	1	1	0.001
O	3	3	2	0.001
O_2	1	1	1	0.25

mass diffusivity has to be specified to describe the transport of species due to diffusion. The diffusion of the species is therefore important because the mass motion of the species is put together by the mass motion of the mixture and the diffusion velocity of the species. A gas with more than two species requires an effective binary diffusion model. This model, which is chosen for the simulations where real gas effects are considered, allows different species to diffuse at different rates with the use of a multicomponent diffusion coefficient.

IV. Results

A. Flowfield Around the Spiked Nose Cone

Generally, great effort is spent to get a flowfield that is not separating from, but attached to, the investigated body. This thought has to be put aside when the benefits of flow-separating aerospikes are examined. The area of recirculating flow in front of the blunt nose cone represents the solution of the complicated problem of drag and heat-transfer reduction, which becomes severe at hypersonic velocities.

The flow, induced by the aerospike, separates due to the pressure rise in front of the nose cone, which exceeds the maximum allowable rise for an attached laminar boundary-layer flow. The size of the recirculation area is dependent on the freestream Reynolds number, and the length of the spike and shape of the tip both have an especially great influence on the shape of the recirculation area. When comparing the flowfields in Figs. 11 and 12, it can be seen that the recirculation area clearly changes shape when different lengths and shapes are used for the attached aerospike.

The region in which the flow is recirculating can be distinguished more easily when examining the lower half of the aerospike assembly in Figs. 11 and 12. The brighter layer represents the shear layer of the recirculation area. The size and shape of this area is controlled by varying both the length of the spike and its shape. Figure 13 shows a more detailed view of the recirculation area with the streamlines in the flowfield being activated. Actually, a second recirculation region is developing, which can be seen when looking

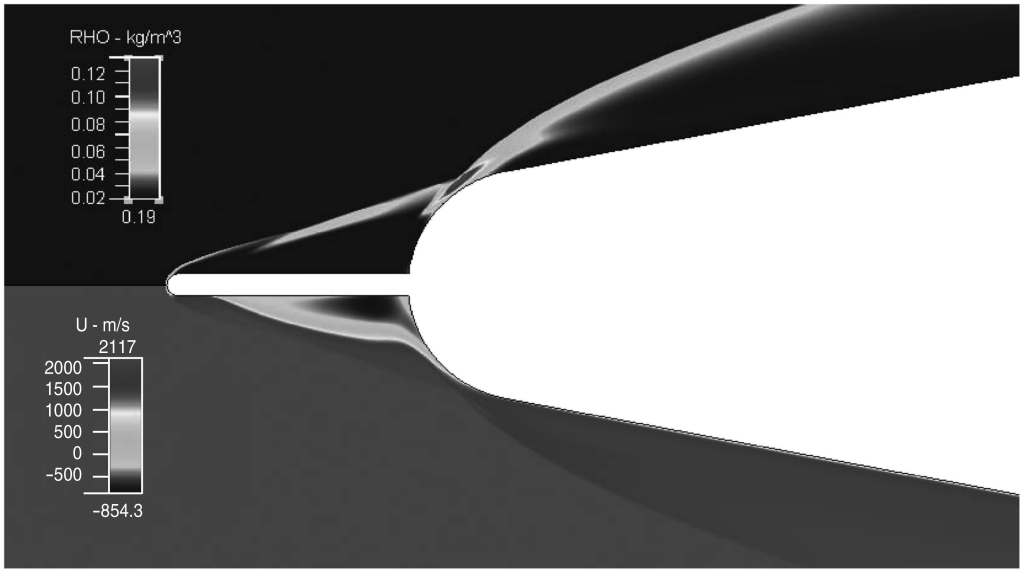

Fig. 11 Flowfields around the spiked nose cone with the blunt spike with $L/D = 1$ at Mach 7.

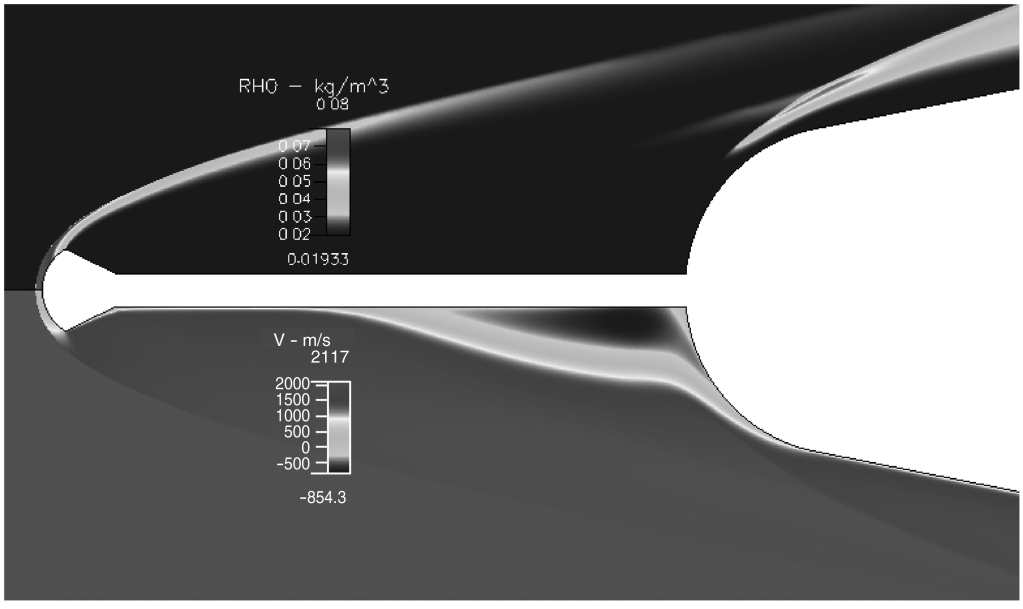

Fig. 12 Flowfields around the spiked nose cone with the aerodome with $D/d = 4$ and $L/D = 1$ at Mach 7.

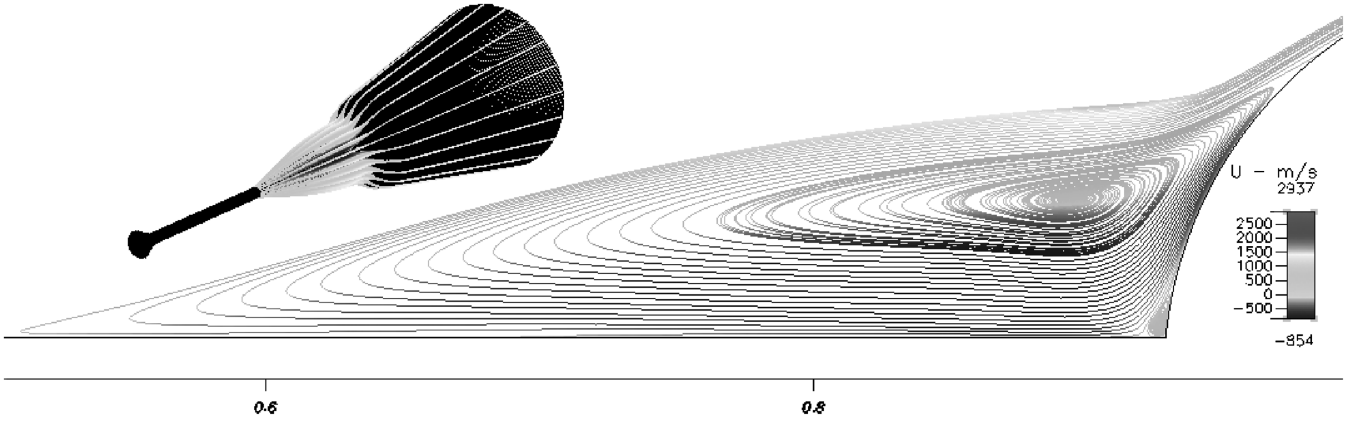

Fig. 13 Recirculation area in front of the nose cone initiated by the aerodome.

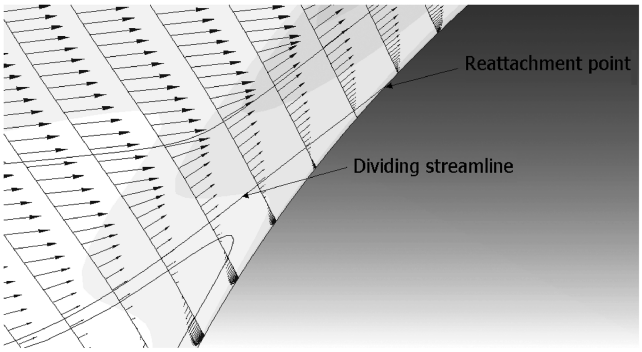

Fig. 14 Dividing streamline and reattachment point of the recirculating flow.

closer at the tip region of the dome in the two-dimensional illustration. This area is characterized by a low subsonic, incompressible Mach regime, that is, below a Mach number of approximately 0.2.

The three-dimensional illustration in the upper left corner shows where the recirculation area is located when the whole assembly is contemplated. The small lines on the surface of the nose cone are the streamlines which "exit" the recirculation cone (they can be seen as lines in the illustration only because several sections of the three-dimensional cone are shown).

As shown in Fig. 14, the streamline representing the shear layer does not touch the body, it proceeds again back to the tip of the dome. In contrast, the dividing streamline has to touch the body at the reattachment point. This point indicates the upper edge of the recirculation region.

With the dividing streamline meeting the body, it can thus be concluded that the outer part of the shear layer passes the reattachment point and proceeds along the aft body. With this happening close to the shoulder of the dome, the result will be less deflection of the outer stream. Consequently, the pressure rise in the reattachment area will be smaller because the flow is now required to be turned with less deflection parallel to the body. Hence, with the reattachment point moving closer to the shoulder, the pressure ratio between the pressure of the recirculation region and the pressure just outside the shear layer will decrease. Furthermore, this decrease also has a positive influence on the heat loads applied onto the surface in the reattachment region. Hence, for the case with the described flow characteristic near the reattachment point, a very good drag reduction and a lower heat load onto the nose cone can be expected.

For a separating flow, the skin friction coefficient is zero at the separation point and the pressure gradient is increasing, that is, it is positive. The investigations emphasize that with increasing spike length the pressure gradient for the separation of the flow becomes smaller, no matter which spike shape is chosen. When plotted over L/D, the pressure gradient with increasing spike length shows the trend of logarithmically approaching a specific value. This can be related to the angle of separation of the laminar boundary layer, which becomes smaller the longer the examined spike length. The difference between the Mach 5 and 7 gradients, which can be emphasized, is related to the changing Reynolds number; it should be noted that the Reynolds number for Mach 5 is 2 times bigger than the one for Mach 7. The dependency on spike length and on Reynolds number is in good agreement with Crawford's [6] results, which concluded that the angle of separation is a weak function of the Reynolds number but more dependent on the spike length.

Wood [7] stated that an increase of the recirculation area temperature, enabled by increasing the wall temperature, corresponds to a decrease in the reattachment pressure rise, which leads to an outward movement of the reattachment point. In the investigated cases, the temperature of the recirculation area increases by approximately 700 K when proceeding from mission point I to III. However, because the freestream Reynolds number changes significantly between mission point I and III, the shape of the recirculation area changes as well, and the reattachment point is not moving closer to the shoulder. This can mainly be ascribed to the changing shock angle induced from the tip of the aerospike, which causes an impingement of the shock front onto the dome for the Mach 10 case with the blunt spike and the sharp spike in particular.

Further properties of the spiked-induced flowfield are two more shocks. The recirculation area causes a deflection of the flow, which leads to a second shock. The angle of this conical shock wave depends on the angle of the shear layer related to the shaft of the spike or, in other words, the half-angle of the conical recirculation region. Dependent on the investigated geometry and the chosen mission point, the flow separation shock can interfere with the bow shock and the reattachment shock. The last shock comes from the deflection of the flow through the blunt dome after passing the reattachment point of the recirculation area. Dependent on the previous flow characteristics, that is, the shape of the bow shock and the size of the recirculation area, this shock can vary significantly. As a matter of course, as the deflection lessens, the bigger the size of the recirculation area is. This can be seen when comparing the flowfields illustrated in Figs. 11 and 12.

B. Blunt Spike

The pressure distribution for the blunt spike with $L/D = 1$ and 4 is plotted in Fig. 15. This should make it easier for the reader to see how significantly the size of the separation area with increasing spike length is changing. The tip of the dome of the nose cone is at $x = 0$, and the pressure ratio p/p_∞ along the wall is plotted on the y axis.

The pressure rise occurring at the tip of the spike is plotted for the blunt spike with $L/D = 1$ and is equal for the other lengths. This pressure rise at the front of the blunt spike is ascribed to the blunt tip of the spike and has to have the same value as the stagnation point pressure rise of the unspiked nose cone. The pressure is increasing more rapidly at the separation point for $L/D = 1$ because the separation angle is bigger. This can be ascribed to the short spike

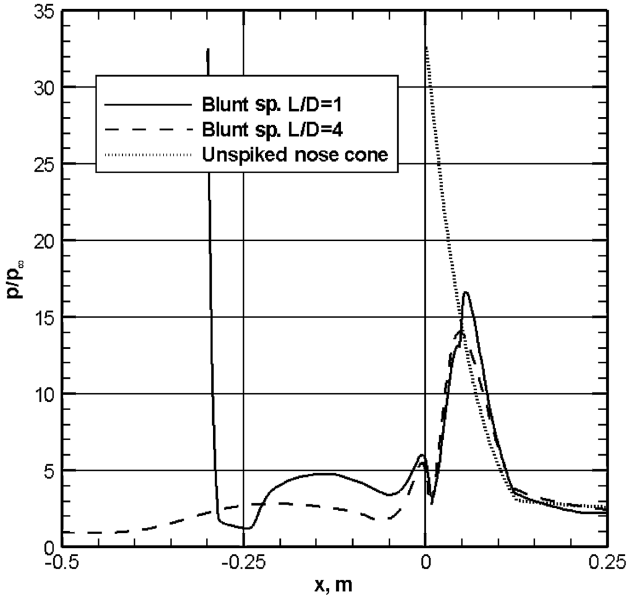

Fig. 15 Pressure distribution along the wall for the blunt spike with $L/D = 1$ and 4, $M = 5$.

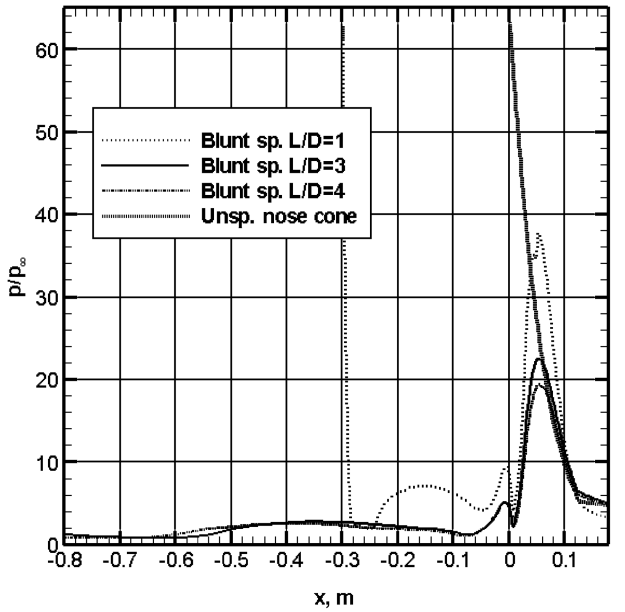

Fig. 16 Pressure distribution along the wall for the blunt spike with $L/D = 1$, 3, and 4, $M = 7$.

length. After a pressure decrease, the next significant pressure rise can be noticed occurring shortly before $x = 0$, which represents the tip of the dome. This comes from the recirculating flow streaming to the tip of the dome, being compressed there and deflected by the shaft of the spike. No shock is occurring due to this deflection because the flow in this region is subsonic.

The pressure peak, which follows the reattachment point for the spike with $L/D = 1$, comes from the impingement of the shear layer onto the surface of the nose cone. For the longer spikes, however, the angle of the separation region is getting smaller, thus the deflection of the flow is less and the flow separation shock gets weaker. Because the separation occurs at a bigger distance from the dome, the flow separation shock does not impinge on the surface. In addition, the front bow shock does not interfere with the other shocks, which leads all in all to a barely detectable pressure rise after the reattachment point.

No big differences can be seen between the pressure distributions for the blunt spike with $L/D = 2$ and 3, which are therefore not plotted in the graph. The similarity of the curves and stagnation points of the recirculation area also clarifies that the size and shape of the recirculation area has to be similar, which can also be seen when comparing the almost equal percentage in drag reduction listed in Table 4.

It can be expected that the blunt spike investigated with the Mach 7 freestream conditions delivers similar pressure distributions along the wall and thus a similar trend in drag reduction. The pressure distribution for $L/D = 1$, 3, and 4 is plotted in Fig. 16. However, the pressure ratio p/p_∞ along the wall is now almost doubled when compared with the Mach 5 results due to the increase of the freestream Mach number. As can be seen in Fig. 16, the separation points already differ remarkably between the spike with $L/D = 1$ and 3. Although the reattachment point is approximately in the same region, the distance between both separation points and the following described effect results in almost 20% more drag reduction obtained by the $L/D = 3$ spike.

Additionally, it can be seen that the pressure peak, occurring after the reattachment point on the surface of the nose cone, is approximately 30% smaller for the longer spike. A further increase of the recirculation area can be noticed with the longest spike. This results in a quite remarkable maximum drag reduction of almost 53%.

Further decreasing shock angles can be expected for the Mach 10 results, which can lead to a severe impingement of the front and the flow separation shock onto the surface of the nose cone. When following the pressure distribution of the shortest spike in Fig. 17, it can be seen that the pressure along the dome of the nose cone exceeds at its peak the stagnation point pressure of the unspiked nose cone. This intense pressure rise is the result of an impingement of both shocks on the dome. The pressure peak for the blunt spike with $L/D = 2$ (not shown in the graph) is also very high when compared with the cases with lower Mach numbers. The shock front is still impinging on the surface, this time further upstream where the inclination of the surface to the impinging shock is less.

However, the results for mission point III have to be treated very carefully because the boundary-layer thickness is getting very large, which may lead to interaction effects. The thickness of the boundary layer depends on the inverse power of the unit Reynolds number and is among other things proportional to the square root of the running length. The unit Reynolds number is roughly 165 times bigger for the mission point II conditions. This means in turn that the boundary layer is $\sqrt{165} \approx 13$ times bigger for the mission point III conditions. This leads to a boundary-layer thickness that has more than 2 times the diameter of the spike at a running length of $x = 0.9$ m ($L/D = 4$).

Additionally, a cold wall case is assumed, which leads to lower temperatures at the wall than an insulated one would experience. The pressure in the boundary layer can be assumed to be constant, that is, $dp/dy \approx 0$. Thus, the equation of state $\rho = p/RT$ yields a higher density in the boundary layer for the cold wall case. This in turn leads to a thinner boundary layer because the mass flow can be

Table 4 Drag reduction of the blunt spike and the sharp spike for all investigated mission points

	Mach 5 blunt spike drag redct., %	Mach 7 blunt spike drag redct., %	Mach 10 blunt spike drag redct., %	Mach 5 sharp spike drag redct., %	Mach 7 sharp spike drag redct., %
$L/D = 1$	31.37	27.48	2.27	27.64	13.80
$L/D = 2$	33.20	44.76	15.26	32.34	19.01
$L/D = 3$	33.84	47.83	24.12	33.50	32.43
$L/D = 4$	37.98	52.57	34.29	35.15	33.05

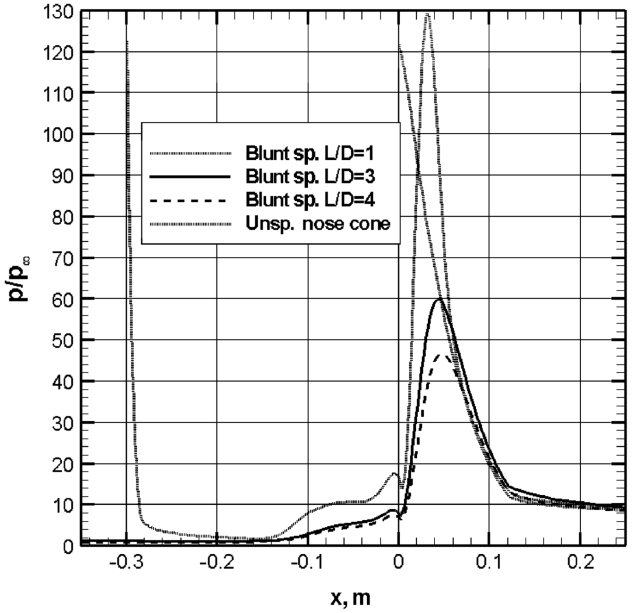

Fig. 17 Pressure distribution along the wall for the blunt spike with $L/D = 1$, 3, and 4, $M = 10$.

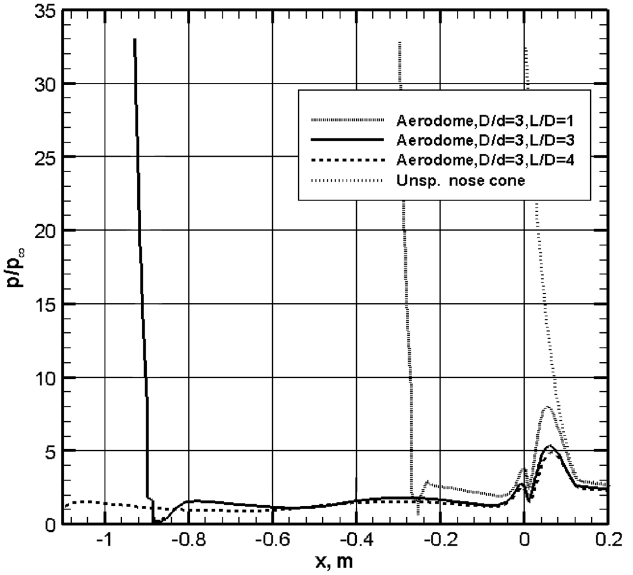

Fig. 18 Pressure distribution along the wall for the aerodome with $D/d = 3$ and $L/D = 1$, 3, and 4, $M = 5$.

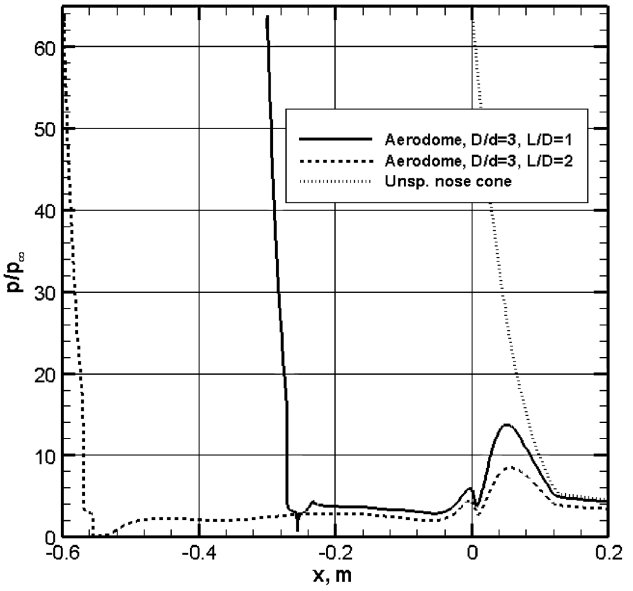

Fig. 19 Pressure distribution along the wall for the aerodome with $D/d = 3$ and $L/D = 1$ and 2, $M = 7$.

accommodated within a smaller one. As the temperature is very high when reaching mission point III and the vehicle is already flying since approximately 50 s, an increase of the wall temperature and thus an even thicker boundary layer can be assumed. Woods's theoretical results showed that an increasing spike temperature also results in a slight increase of the separation angle, thus the separated flow region gets bigger. Hence, an increase of T_w may cause an earlier and even more unpredictable interaction with the shocks as is already the case.

C. Sharp Spike

The graphs of the pressure distribution look very similar to the ones of the blunt spike and are therefore not illustrated. The size of the recirculation area is almost equal to the one initiated by the blunt spike, which results in similar values of the drag reduction when compared with the blunt spike (see Table 4). The difference of the pressure distribution between the spike with $L/D = 3$ and 4 is hardly recognizable. It can be concluded that the sharp spike reaches the maximum of its beneficial effect at mission point I, when the length $L/D = 3$ is being exceeded.

When looking at the drag reductions of the sharp spike at mission point II conditions, the result shows a more noticeable difference this time when compared with the blunt spike. The percentage of the drag reduction for the shorter spikes shows that more pressure is applied on the dome's surface when proceeding from mission point I to II, which leads to a higher drag. In addition, the drag reduction for the sharp spike, when comparing the results of mission point I to II, shows the opposite trend than the blunt spike for which a further decrease could be achieved. Again, the spike with $L/D = 3$ delivers roughly the same drag reduction than the longest spike.

As a matter of fact, the shape of the tip of the spike is the reason why a recirculation area with a different separation angle develops. The sharp spike causes a detached shock wave with a much smaller stand-off distance than the blunt spike. Thus, the shock front proceeds closer to the body. The separation angle α for the recirculation area of the sharp spike ($\alpha \approx 12$ deg) is 8 deg smaller than the one for the blunt spike with $\alpha \approx 20$ deg, which may be ascribed to the stronger bow shock. This leads to a significantly smaller size of the recirculation area because the reattachment point is then located much closer to the tip of the dome. This causes a high deflection for the incoming shear layer, which results in a higher pressure on the dome. This fact is more obvious when $L/D = 2$ is considered. Here the recirculation area covers 41% of the sharp spike, whereas 77% of the blunt spike is surrounded by the adverse flow. This results in more than a double reduction of drag for the blunt spike.

The numerical computations for the sharp spike with the mission point III freestream conditions are not conducted. The adverse trend and the closer shock front explained in this section, and the results from the blunt spike with Mach 10, let us assume that especially for the shorter spikes, that is, $L/D \leq 2$, a significant beneficial effect of the sharp spike cannot be expected.

D. Aerodome with $D/d = 3$

The aerospike with the aerodome mounted on the tip yields a different located shock front compared with the previously investigated spikes. It is obvious that this also results in different pressure distributions along the surface, when compared with the previously shown graphs, as shown in Figs. 18–20.

The most important and significant difference is that the pressure peak on the dome is highly reduced. The maximum pressure occurs as a matter of course in the stagnation point of the aerodome, but the pressure on the dome this time is remarkably lower than exhibited by

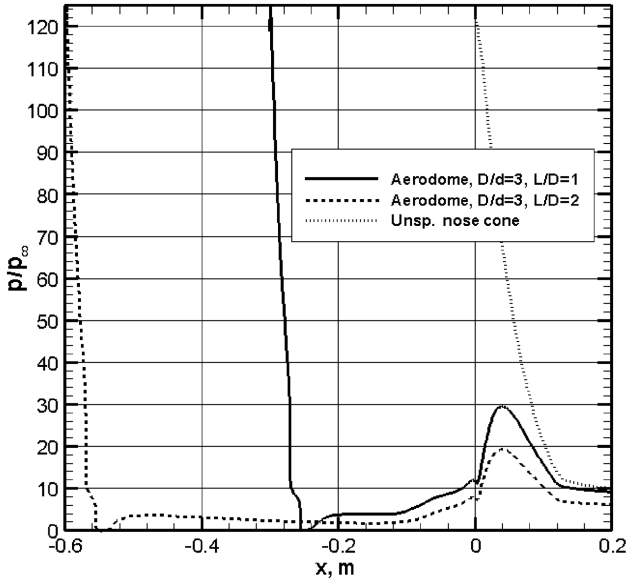

Fig. 20 Pressure distribution along the wall for the aerodome with $D/d = 3$ and $L/D = 1$ and 2, $M = 10$.

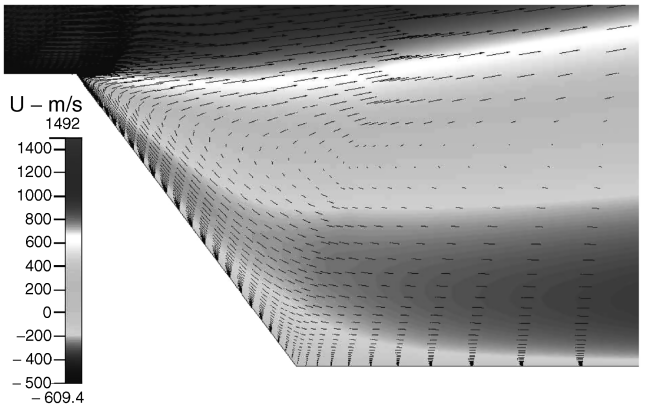

Fig. 21 Velocity distribution and vectors in the flowfield behind the aerodome with $L/D = 1$, $M = 5$.

the blunt or the sharp spike. For these spikes, the worst case for mission point I results in a peak of the pressure ratio p/p_∞ on the dome of approximately 50% of the stagnation point value. When glancing at the graph in Fig. 18, it can be seen that the pressure peak on the dome is reduced to just ~25% of the stagnation point value when the aerodome with $D/d = 3$ and $L/D = 1$ is assembled. A further reduction can be noticed for the longer spikes. However, the pressure distribution resulting from the aerodome shows no significant changes from the spike length for $L/D = 2$ upwards.

The flowfield resulting from the spikes with $L/D = 1$ and 2 should be further explained because they exhibit a very interesting recirculation area. As can be assumed from the pressure distribution on the frontal area of the spike in Fig. 18, there occurs no smooth separation induced from the increasing pressure gradient dp/dx as was previously examined. The almost straight pressure gradient at the front (starting at approximately $x = -0.25$ for the spike with $L/D = 1$) is ascribed to the recirculating flow being deflected by the aft side of the aerodome.

There occurs no expansion as expected. Figure 21 emphasizes that the expansion of the flow passing the aerodome is inhibited by the recirculating flow, which causes the incoming flow to proceed along the developed recirculation area. Thus, the complete area between the aft side of the aerodome and the nose cone exhibits a recirculating flow.

The flowfield for the spike with $L/D = 2$ looks similar, that is, the shaft of the spike is covered equally as well by a recirculation area,

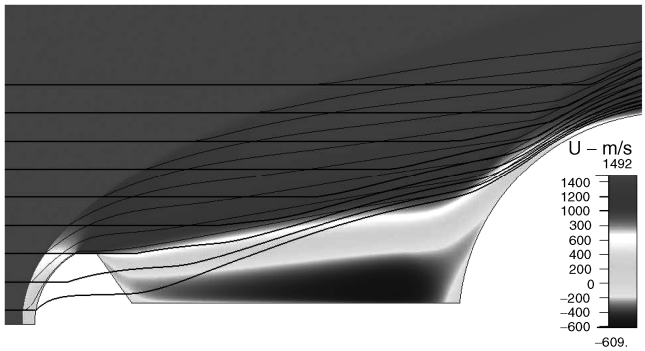

Fig. 22 Velocity distribution for the aerodome, and streamlines for the aerodome (thin) and the blunt spike (thick).

but behind the aerodome occurs a slight expansion that brings the dividing streamline at the front closer to the shaft when compared with the shorter spike. This means that the recirculation area is approximately doubled in its size.

A further important conclusion may be drawn when examining the streamlines proceeding through the bow shock. The freestream is basically deflected by the aerodome and its strong induced bow shock, which can be seen when following the streamlines in Fig. 22. For a better comparison the streamlines for the aerodome (thin lines) and the blunt spike (thick lines) are plotted simultaneously.

The flow far from the aerodome is still significantly deflected when proceeding through the bow shock. This results in the fact that the flow is not forced to transport the same mass through a significantly smaller area as is the case for the blunt spike. This compression of the flow causes a significant pressure, rise which will be shown shortly.

To explain the increase of the pressure peak on the nose cone when the blunt spike is assembled, the law of mass conservation may be applied with

$$\rho_1 u_1 A_1 = \rho_2 u_2 A_2 \tag{3}$$

The left-hand side of the equation describes the freestream condition. The area is defined through the upper and lower streamlines shown in Fig. 22. The right-hand side describes the state of the flow where the upper streamline just passes the reattachment shock above the nose cone. The freestream density, velocity, and the area through which the streamlines flow have the same value in both cases, thus for the blunt spike Eq. (3) can be equated with the one for the aerodome that yields

$$(\rho_2 u_2 A_2)_{\text{aerodome}} = (\rho_2 u_2 A_2)_{\text{blunt spike}} \tag{4}$$

Furthermore, the averaged velocity u_2 can be assumed to have the same value in both cases, because the front shock causes no significant decrease in the velocity, and the shape of the second shock is similar. The area A_2 for the blunt spike is approximately halved when compared with the area, which has to be surpassed by the streamlines in the flowfield of the aerodome or, in another notation, $A_{2,\text{blunt sp.}} \approx 0.5 A_{2,\text{aerod.}}$. Substituting this relation in Eq. (4) results in $\rho_{2,\text{blunt sp.}} = 2\rho_{2,\text{aerod.}}$. With the equation of state $p = \rho RT$ and the assumption that the temperature T_2 is equal in both cases, it results $\rho_{2,\text{blunt sp.}} = 2\rho_{2,\text{aerod.}}$. When comparing the pressure distribution of the blunt spike plotted in Fig. 15 with the one of the aerodome with $L/D = 1$ in Fig. 18, it can be seen that the pressure peak on the nose cone is indeed double the size of the one occurring for the aerodome. Thus, it can be concluded that the stronger bow shock induced by the aerodome has a more beneficial effect than the weaker one resultant from the blunt spike.

Although the values do not significantly increase, a further reduction of drag can be achieved by the longer spikes. With the longer spikes, it shows that the shaft is not completely surrounded by the recirculation area but that this area still covers half of the shaft and is characterized by a small conical apex angle. There is also another difference that should be briefly explained when comparing the

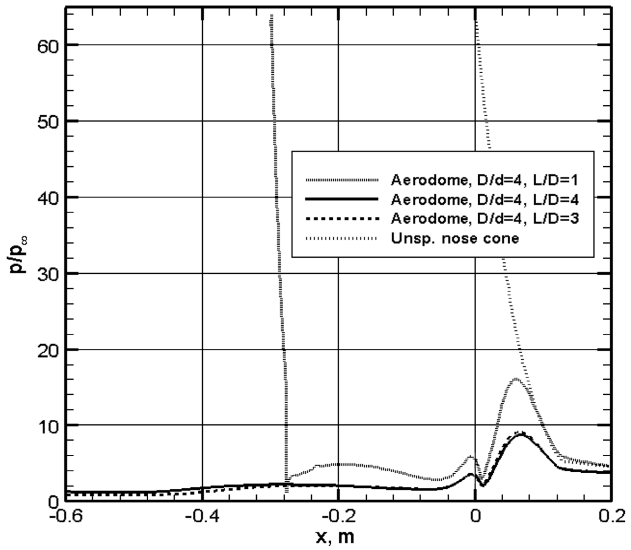

Fig. 23 Pressure distribution along the wall for the aerodome with $D/d = 4$, $L/D = 1$, and $L/D = 3$ and 4, $M = 7$.

exhibiting flowfield of the spikes with $L/D \geq 3$ to the shorter ones. In this case an expansion occurs on the aft side of the aerodome. Because the deflection is too big for the flow to remain attached, another small recirculation area is formed there. The pressure peak on the dome shows a further decrease when compared with the $L/D = 1$ spike and only a slight decrease when compared with the $L/D = 2$ spike. Thus, again, a further increase in spike length, that is, longer than $L/D = 2$, shows no further significant beneficial effects.

The pressure distribution shows the same trend for the mission point II results. Only the spike with $L/D = 1$ exhibits a recirculation area that surrounds the whole shaft of the spike. However, the strong deflection of the bow shock induced from the aerodome leads to the same drag-reducing effect as described previously.

For mission point III, the longer spikes, that is, $L/D > 2$, are not calculated because the aforementioned thickening of the boundary layer leads to results that are not accurate enough. Furthermore, even the shaft of the spike with $L/D = 1$ is now no longer completely surrounded by a recirculating flow. The same phenomenon is exhibited as seen with the previously investigated spikes, namely, that the point of separation does not proceed along the shaft closer to the aerodome with an increase in spike length.

E. Aerodome with $D/d = 4$

The flowfield of the shortest spike with the mission point I freestream conditions is again characterized by a recirculation area that surrounds the whole shaft and the aft side of the aerodome. The flow above the conical aft side proceeds parallel to the shaft and then, as the angle of the dividing streamline is increasing, is slightly deflected along the recirculation area. Although the diameter of the aerodome is now reduced to $D/d = 4$, the front bow shock is still strong enough to deflect the flow significantly so that the pressure applied along the surface of the nose cone is highly reduced.

A further important result can be drawn out of the pressure distribution, namely, that for both sizes of the aerodome no severe impingement of the bow shock on the nose cone occurs (see Fig. 23). Table 5 shows that the aerodome with the shortest spike length

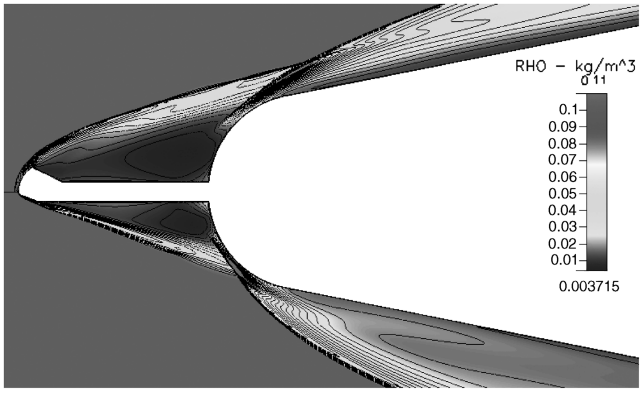

Fig. 24 Comparison of the flowfield with Mach 7 freestream conditions induced from the aerodome with $D/d = 4$ and the sharp spike with $L/D = 1$.

already achieves a drag reduction of 50% at mission point II conditions. Table 5 again confirms the trend that the spike length exceeding $L/D = 3$ results in only a slight increase of the obtained drag reduction.

The aerodome with $D/d = 4$, which delivers the highest drag reduction for the spike length $L/D = 1$, is compared in Fig. 24 with the sharp spike delivering the smallest. The most obvious difference can be seen in the bow shock, which is proceeding much closer to the body in the lower half of the illustration. This results in the impingement on the nose cone that leads to 36% less drag reduction for the sharp spike. The flow separation shock for the aerodome merges with the bow shock and proceeds at a reasonable distance along the nose cone. Its reflection through the reattachment shock is visible in the s-formed density contours. It should be pointed out that the exhibited recirculation area for the sharp spike simply cannot be bigger in its size because the area is limited by the small half-angle of the spike-induced bow shock.

F. Summary

The results for the drag reduction of all performed simulations are summarized in Figs. 25 and 26. Apparently, the increasing drag reduction by extending the spike length from 1 to 4 times the diameter of the dome is the most obvious trend. When comparing both figures, one can see that the spike with the aerodome at the tip exhibits a higher drag reduction level than the blunt and especially the sharp spike. Figure 26 in particular emphasizes that the relative increase in drag reduction is decreasing when proceeding from $L/D = 1$ to 4. For all spikes, it is seen that the drag reduction is increasing from mission point I to II and then decreasing again at mission point III conditions, where the separation point is not proceeding further away from the nose cone when the spike is extended. Additionally, it is the latter mission point for which the smallest values for the drag reduction are obtained. This can basically be related to the shock front being located closer to the body compared with the mission points in lower altitudes and the stagnating separation point.

G. Heat Transfer

Figures 27 and 28 illustrate the percentage reduction of the maximum occurring heat load applied on the nose cone's surface

Table 5 Percentage of drag reduction for the aerodome shapes

	Mach 5 aerod. $D/d = 3$ drag redct., %	Mach 7 aerod. $D/d = 3$ drag redct., %	Mach 10 aerod. $D/d = 3$ drag redct., %	Mach 5 aerod. $D/d = 4$ drag redct., %	Mach 7 aerod. $D/d = 4$ drag redct., %	Mach 10 aerod. $D/d = 4$ drag redct., %
$L/D = 1$	37.68	42.98	30.24	42.14	49.24	26.02
$L/D = 2$	47.94	56.52	42.95	46.24	57.37	40.37
$L/D = 3$	50.14	58.93	——	48.50	61.72	——
$L/D = 4$	53.22	62.30	——	48.80	62.73	——

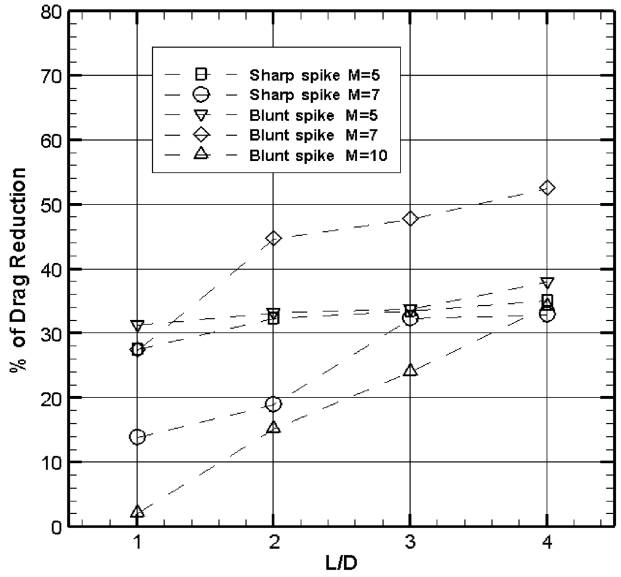

Fig. 25 Percentage of drag reduction for the sharp and the blunt spikes.

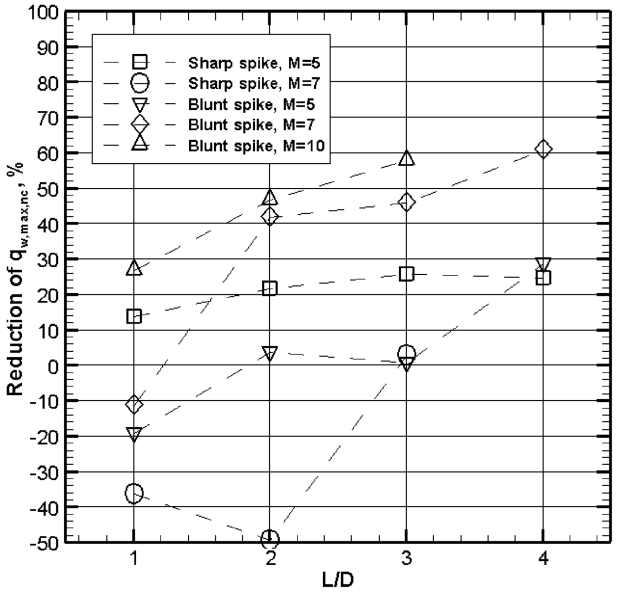

Fig. 27 Percentage of heat-transfer peak reduction on the nose cone for the sharp and the blunt spikes.

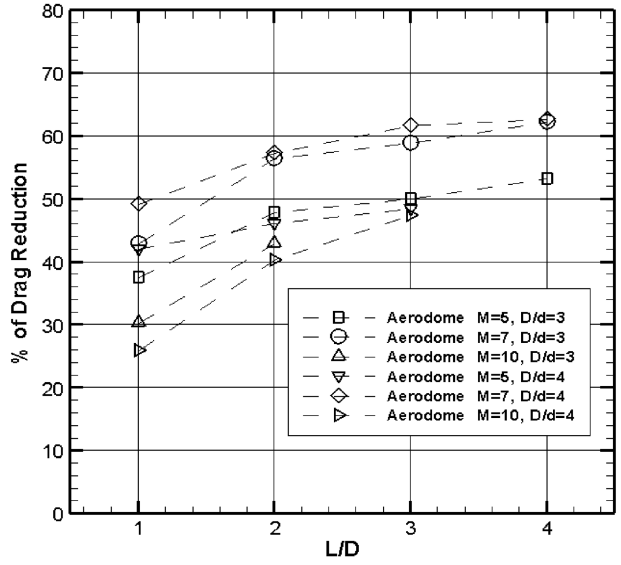

Fig. 26 Percentage of drag reduction for the aerodome with $D/d = 3$ and 4.

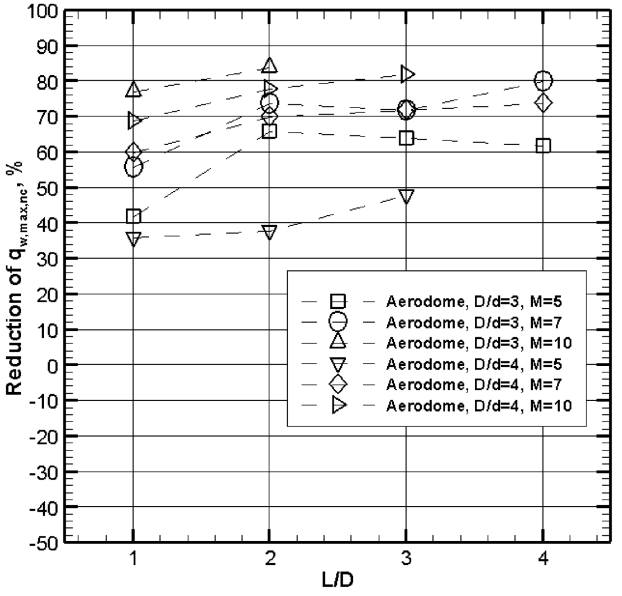

Fig. 28 Percentage of heat-transfer peak reduction on the nose cone for the aerodome with $D/d = 3$ and 4.

$q_{w,\max,\mathrm{nc}}$ when spikes are attached. Although the graphs show some discrepancies, a clear trend can be seen of a further reduction of the maximum heat load when the spike length is extended. For every shape investigated, the reduction obtained at mission point III conditions yields the smallest peak on the nose cone's surface. This is consistent with the investigations conducted by Bogdonoff and Vas [4], who also obtained a decreasing peak by increasing the freestream Mach number. In some cases, the reduction again slightly decreases when the spike is extended from $L/D = 3$ to 4. However, the reduction obtained in the heat load peak when the aerodome is mounted on the nose cone is remarkable. With a maximum reduction of 85%, the aerodome delivers 20% more reduction than that obtained by the best blunt spike configuration. Although the majority of the cases lead to a reduction of the heat transfer, some cases result in a peak increase, as can be seen in the lower half of Fig. 27. The sharp spike with a length smaller than $L/D = 3$, in particular, results in a mentionable heat load increase due to a severe shock impingement.

It should be noted that some caution is warranted as computations are conducted with a laminar flow model, whereas investigations conducted by Stalder and Nielsen [3] with lower supersonic speeds of spiked hemisphere cylinders showed that the increased heat transfer on their investigated models may be caused by repeated impingement of the turbulent separated region into the outer edge of the boundary layer on the body nose. However, they were not sure if this was the correct physical explanation for the increase in heat transfer.

For the blunt spike, the first significant beneficial effects in terms of heat transfer occur at mission point II. The shortest spike delivers for the first two mission points a heat flux increase on the nose cone, whereas a 60% reduction of the maximum occurring heat flux on the nose cone can be achieved with the longest spike at mission point II. At mission point III, the fully catalytic wall assumption yields a 9% increase of both the stagnation point heat transfer and the maximum heat flux on the nose cone compared with the simulations with nonreacting flows.

The sharp spike results in a 73% higher stagnation point heat flux when compared with the blunt spike. Although the sharp spike yields

a maximum reduction of 26% at mission point I, this shape of the spike is definitely not recommended.

Although the stagnation point heat transfer for the aerodome is higher than the unspiked, one this shape provides throughout the mission points and lengths an absolutely remarkable heat-flux reduction level. The fully catalytic wall assumption again leads to a 12% increase of the stagnation point heat transfer and a 6.5% increase of the maximum heat transfer on the nose cone.

V. Conclusions

The drag and the heat-transfer reduction of a forward-facing spike with varying length and shape in comparison to the unspiked nose cone have been numerically investigated at three chosen mission points at which the vehicle is flying with hypersonic velocities.

Depending on the spike length and mission point, the blunt spike delivers a drag reduction in the range of 2% for the shortest spike at mission point III up to 53% for the longest spike at mission point II. The blunt spike with $L/D = 1$ induces a conical bow shock, which begins to impinge on the surface of the nose cone somewhere on the trajectory between mission point II and III.

The sharp spike delivers the lowest level of drag reduction with a maximum of 35% for the longest spike at mission point I. However, due to the sharp tip of the spike, a shock with a smaller shock angle is exhibited when compared with the blunt spike. This results in an even more severe impingement of the bow shock, which can now also be noticed for the sharp spike with $L/D = 2$. Because of those facts, a beneficial effect of the sharp spike cannot be expected at mission point III conditions.

A remarkable drag reduction level can be achieved with the aerodome with $D/d = 3$ mounted onto the nose cone reaching from 30% up to 62%. No impingement can be noticed. No significant increase of the drag reduction can be obtained when the spike length of the aerodome exceeds $L/D = 2$.

No fewer stunning results can be obtained by the spike with the smaller aerodome with $D/d = 4$ mounted on the tip of the spike. This shape provides the highest drag reduction that could be obtained with the shortest spike at mission point I conditions. The margin reaches from 26% for mission point III and $L/D = 1$ up to 63% for mission point II and $L/D = 4$. The two aerodome shapes exhibit an interesting flowfield for the shortest spike at the first two mission points. The whole shaft of the spike is surrounded by a recirculation area that yields the highest effectivity.

If a blank spike should be used, the author recommends the usage of the blunt spike with a length of at least $L/D = 2$. The shortest spike should be avoided because this length can lead to the same impingement location of both the bow shock and the reattachment shock. However, the best results can be obtained with both aerodome shapes. The shortest spike is in many cases as beneficial as the longest blunt spike if not even more advantageous. The diameter of the aerodome has to be chosen dependent on the needed drag or heat-transfer reduction. The author recommends the usage of the aerodome up to a length of $L/D = 2$ because the extension above this length delivers only tiny further beneficial results.

In June 2007, the aerodome with $D/d = 4$ and $L/D = 2$ proved its usage in flight on the tip of the HyCAUSE nose cone. The drag reduction was achieved as calculated and the rocket reached its predefined apogee.

References

[1] Myrabo, L., and Raizer, Y. P., "Laser Induced Air Spike for Advanced Trans-Atmospheric Vehicles," AIAA Paper 94-2451, 1994.

[2] Meyer, B., Nelson, H. F., and Riggins, D. W., "Hypersonic Drag and Heat-Transfer Reduction Using a Forward-Facing Jet," *Journal of Aircraft*, Vol. 38, No. 4, 2001, pp. 680–686.

[3] Stalder, J. R., and Nielsen, H. V., "Heat Transfer from a Hemisphere-Cylinder Equipped with Flow-Separation Spikes," NACA TN 3287, 1954.

[4] Bogdonoff, S. M., and Vas, I. E., "Preliminary Investigations of Spiked Bodies at Hypersonic Speed," *Journal of the Aerospace Sciences*, Vol. 26, No. 2, 1959, pp. 65–74.

[5] Chapman, D. R., "A Theoretical Analysis of Heat Transfer in Region of Separated Flow," NACA TN 3792, 1956.

[6] Crawford, D. H., "Investigation of the Flow over a Spiked-Nose Hemisphere Cylinder at a Mach Number of 6.8," NASA TN D-118, 1959.

[7] Wood, C. J., "Hypersonic Flow over Spiked Cones," *Journal of Fluid Mechanics*, Vol. 12, Pt. 4, 1962, pp. 614–627. doi:10.1017/S0022112062000427

[8] Reding, J. P., Guenther, R. A., and Richter, B. J., "Unsteady Aerodynamic Considerations in the Design of a Drag-Reduction Spike," *Journal of Spacecraft and Rockets*, Vol. 14, No. 1, 1977, pp. 54–60.

[9] Hutt, G. R., and East, R. A., "Static and Dynamic Pitch Stability of a Blunted Cone with Forward Facing Aerodynamic Spike in Hypersonic Flow," *Aeronautical Journal*, Vol. 89, No. 888, 1985, pp. 307–314.

[10] Huebner, L. D., Mitchell, A. M., and Boudreaux, E. J., "Experimental Results on the Feasibility of an Aerospike for Hypersonic Missiles," AIAA Paper 95-0737, 1995.

[11] Shoemaker, J. M., "Aerodynamic Spike Flowfields Computed to Select Optimum Configuration at Mach 2.5 with Experimental Validation," AIAA Paper 90-0414, 1990.

[12] Fujita, M., and Kubota, H., "Numerical Simulation of Flowfield over a Spiked Blunt Nose," *Computational Fluid Dynamics Journal*, Vol. 1, No. 2, 1992, pp. 187–195.

[13] Yamauchi, M., Fujii, K., Tamura, Y., and Higashino, F., "Numerical Investigation of Supersonic Flows Around a Spiked Blunt Body," *Journal of Spacecraft and Rockets*, Vol. 32, No. 1, 1995, pp. 32–42; also AIAA Paper 93-0887, Jan. 1993.

[14] Mehta, R. C., "Numerical Heat Transfer Study over Spiked Blunt Bodies at Mach 6.8," *Journal of Spacecraft and Rockets*, Vol. 37, No. 5, 2000, pp. 700–703.

[15] Mehta, R. C., "Numerical Simulation of Self-Sustained Oscillations over Spiked Blunt-Bodies," AIAA Paper 2001-0262, 2001.

[16] Kamran, N., Zahir, S., and Khan, M. A., "Computational Investigation of Blunt Body Drag-Reduction Spikes in Hypersonic Flows," *CFD Conference 2003*, Paper 30 AB4, 2003.

[17] Thurman, W. E., "A Flow-Separation Spike for Hypersonic Control of a Hemisphere-Cylinder," *AIAA Journal*, Vol. 2, No. 1, 1964, pp. 159–161.

[18] Hirschel, E. H., *Basics of Aerothermodynamics*, Springer–Verlag, Berlin/New York/Heidelberg, 2005.

[19] Wilcox, D. C., *Turbulence Modeling for CFD*, 2nd ed., DCW Industries, Inc., La Canada, CA, 1998.

[20] Boyce, R., Neely, A., Odam, J., and Stewart, B., "CFD Analysis of the HyCAUSE Nosecone," AIAA Paper 2005-3339, May 2005.

[21] Klopfer, G. H., and Yee, H. C., "Viscous Hypersonic Shock-on-Shock Interaction on Blunt Cowl Lips," AIAA Paper 88-0233, 1988.

[22] Roache, P. J., *Fundamentals of Computational Fluid Dynamics*, Hermosa Publishers, Socorro, NM, 1998.

[23] Wen, C. Y., Hornung, H. G., "Nonequilibrium Dissociating Flow Over Spheres," *Journal of Fluid Mechanics*, Vol. 299, May 1995, pp. 389–405. doi:10.1017/S0022112095003545

[24] Park, C., "On Convergence of Computation of Chemically Reacting Flows," AIAA Paper 85-0247, 1985.

[25] Vincenti, W. G., and Kruger, C. H., "*Introduction to Physical Gas Dynamics*," Wiley, New York, 1965; reprint, Krieger Publishing Co., Melbourne, FL, 1975.

T. Lin
Associate Editor